Planetary nebulae with Wolf–Rayet-type central stars – I. The case of the high-excitation NGC 2371

V. M. A. Gómez-González,[1]★ J. A. Toalá [ORCID],[1] M. A. Guerrero [ORCID],[2] H. Todt,[3] L. Sabin [ORCID],[4] G. Ramos-Larios [ORCID][5] and Y. D. Mayya[6]

[1]*Instituto de Radioastronomía y Astrofísica (IRyA), UNAM Campus Morelia, Apartado Postal 3-72, 58090 Morelia, Michoacán, Mexico*
[2]*Instituto de Astrofísica de Andalucía (IAA-CSIC), Glorieta de la Astronomía S/N, E-18008 Granada, Spain*
[3]*Institute for Physics and Astronomy, Universität Potsdam, Karl-Liebknecht-Str 24/25, D-14476 Potsdam, Germany*
[4]*Instituto de Astronomía, UNAM, Apdo. Postal 877, Ensenada 22860, B.C., Mexico*
[5]*Instituto de Astronomía y Meteorología, CUCEI, Universidad de Guadalajara, Av. Vallarta 2602, Arcos Vallarta, 44130 Guadalajara, Mexico*
[6]*Instituto Nacional de Astrofísica, Óptica y Electrónica, Luis Enrique Erro 1, Tonantzintla 72840, Puebla, Mexico*

ABSTRACT

We present the analysis of the planetary nebula (PN) NGC 2371 around the [Wolf–Rayet] (WR) star WD 0722+295. Our Isaac Newton Telescope intermediate dispersion spectrograph spectra, in conjunction with archival optical and ultraviolet images, unveil in unprecedented detail the high ionization of NGC 2371. The nebula has an apparent multipolar morphology, with two pairs of lobes protruding from a barrel-like central cavity, a pair of dense low ionization knots misaligned with the symmetry axis embedded within the central cavity, and a high-excitation halo mainly detected in He II. The abundances from the barrel-like central cavity and dense knots agree with abundance determinations for other PNe with [WR]-type central stars of PNe. We suggest that the densest knots inside NGC 2371 are the oldest structures, remnant of a dense equatorial structure, while the main nebular shell and outer lobes resulted from a latter ejection that ended the stellar evolution. The analysis of position–velocity diagrams produced from our high-quality spectra suggests that NGC 2371 has a bipolar shape with each lobe presenting a double structure protruding from a barrel-like central region. The analysis of the spectra of WD 0722+295 results in similar stellar parameters as previously reported. We corroborate that the spectral subtype corresponds with a [WO1] type.

Key words: stars: evolution – stars: winds, outflows – planetary nebulae: general – planetary nebulae: individual: NGC 2371.

1 INTRODUCTION

Planetary nebulae (PNe) represent a short-lived configuration of the circumstellar medium of evolved low- and intermediate-mass stars (1 $M_\odot \lesssim M_i \lesssim$ 8 $M_\odot$). The interacting stellar winds model of formation predicts that low- and intermediate-mass stars evolve through the asymptotic giant branch (AGB) phase producing a dense and slow wind, which eventually will be swept and compressed by the future fast stellar wind of the post-AGB star and subsequently ionized by the newly developed ultraviolet (UV) flux (see Kwok, Purton & Fitzgerald 1978; Balick 1987). The wide variety of PN morphologies (round, bipolar, multipolar, irregular, etc.; see Sahai, Morris & Villar 2011) has led to the suggestion that several agents might contribute to the PN shaping, including binarity (or multiple

systems; Akashi & Soker 2017), jets, and magnetic fields (see the review by Zijlstra 2015).

Central stars of PNe (CSPNe) commonly show the presence of hydrogen in their surfaces. However, about 10 per cent of CSPNe do not exhibit hydrogen features, i.e. they are hydrogen-deficient, rather displaying emission features in their spectra similar to those of the massive Wolf–Rayet (WR) stars of the carbon sequence (see Acker & Neiner 2003; Górny 2001, and references therein). Accordingly, they are classified in the same way as WR stars, just using square brackets to denote that they are CSPNe instead (Tylenda, Acker & Stenholm 1993; Crowther, De Marco & Barlow 1998; Acker & Neiner 2003). It is interesting to note that only a few PNe have been reported to harbour hydrogen-poor [WR] CSPN of the nitrogen sequence: the transitional [WN/WC]-type PB 8 (Todt et al. 2010) and the [WN]-type CSPNe of Abell 48 (Todt et al. 2013a) and IC 4663 (Miszalski et al. 2012).

In general, abundance determination of PNe with [WR]-type CSPNe do not present major differences compared to those classical

★ E-mail: mau.gglez@gmail.com
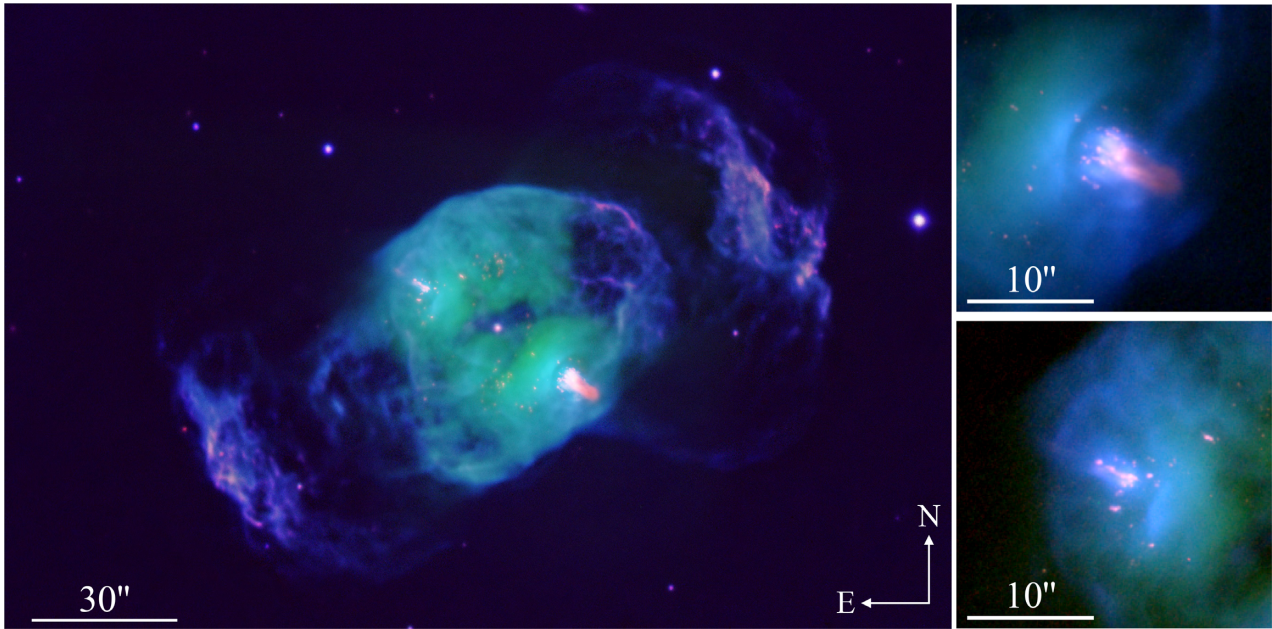
Figure 1. Colour-composite images of NGC 2371. The wide-field image (left-hand panel) was produced by combining the CFHT and *HST* observations. The right-hand panels were obtained by only taking the *HST* observations. In all panels red, green, and blue correspond to [N II], Hα, and [O III], respectively.

PNe with hydrogen-rich CSPNe (e.g. Peña et al. 1998; Peña, Stasińska & Medina 2001). Hydrogen-deficient material ejected inside the old, hydrogen-rich PN has been identified only around a few [WR]-type CSPN (see Guerrero et al. 2018, and references therein). These are known as *born-again* PNe and it is accepted that the CSPN experienced a very late thermal pulse (VLTP) ejecting hydrogen-depleted and carbon-rich processed material (e.g. Herwig et al. 1999; Miller Bertolami & Althaus 2006). Although this evolutionary path has been suggested to explain the formation of hydrogen-poor [WR] stars, it might not apply to all PNe harbouring [WR] stars (see Górny & Tylenda 2000).

Statistical studies of PNe around [WR] CSPNe have shed light into the relation between the nebular properties and the evolutionary sequence of the progenitor stars. For example, the decrease in electron density (n_e) with decreasing spectral subtype has been suggested to be a signature of an evolutionary sequence from the late to early [WC]-type (Acker, Górny & Stenholm 1996; Górny & Tylenda 2000). Furthermore, the N/O abundance ratio versus [WC] class presented by Peña et al. (2001) confirmed the claim that stars with different masses evolve through the same [WC] state (e.g. Peña et al. 1998; De Marco & Crowther 1999).

Comparisons between PNe harbouring non-emission line CSPNe with those hosting [WR] CSPNe have unveiled subtle differences. PNe with [WR] CSPNe are generally more centrally condensed, expand faster, and exhibit a higher degree of turbulence than PNe with non-emission line CSPNe (e.g. Gesicki et al. 2006; Medina et al. 2006; Jacob, Schönberner & Steffen 2013, and references therein). They also seem to have higher N and C abundances, implying that they have evolved from stars with initial masses $\sim$4 M$_\odot$ (García-Rojas et al. 2013). This is consistent with their preferential location at low latitudes in the Galactic disc (Peña, Rechy-García & García-Rojas 2013). Finally, it has been noted recently that PNe with [WC] CSPNe have a higher occurrence of fast collimated outflows than PNe with weak emission line CSPNe or non-emission line CSPNe (Rechy-García et al. 2017).

These statistical studies rely on averaged values of the nebular physical properties (electron density and temperature), abundances, and velocity fields that might hide important clues on the evolution of PNe with [WR]-type CSPNe. For example, dedicated studies of compact [WR] PNe have unveiled the effects of fast collimated outflows in their early shaping (Rechy-García et al. 2017; Rechy-García, Peña & Velázquez 2019). Detailed studies of individual PNe with [WR] CSPNe are clearly needed to understand this unique evolutionary path of low- and intermediate-mass stars. We have therefore started a series of detailed studies of PNe harbouring [WR] CSPNe. In this first paper, we present a study of NGC 2371 (a.k.a. PNG 189.1+19.8; Curtis 1918), which harbours the [WR] CSPN WD 0722+295.

NGC 2371 has been classified as a barrel-like PNe of Peimbert type II (see table 1 in Henry et al. 2018). Morphological studies performed with the *Hubble Space Telescope* (*HST*), *Spitzer*, and ground-based telescopes have unveiled a variety of morphological features (see Fig. 1; Sabbadin, Bianchini & Hamzaoglu 1982; Ramos-Larios & Phillips 2012): two-bipolar lobes extending $\gtrsim$1 arcmin from the CSPN towards the NW and SE directions with position angle PA $\approx$ $-60°$, a main central cavity with an ellipsoidal shape with an extension of 28 arcsec $\times$ 38 arcsec that exhibits a couple of blowout features aligned with the outer lobes, and a collection of dense knots mainly detected in [N II] and [S II] narrow-band filter images (see next section). The two brightest knots are aligned in the NE to SW direction with a PA $\approx$ 60°, but the line that connects them is not perfectly aligned with the CSPN. Ramos-Larios & Phillips (2012) presented a detailed discussion on the properties of the dense NE and SW knots. Their *HST* images show that these are actually conglomerates of clumps (see also Fig. 1). A secondary pair of smaller size clumps is observed at a PA = 5°. It is worth noting that the low ionization clumps do not have a uniform distribution around the CSPN nor are they aligned with the bipolar lobes.

Optical (Torres-Peimbert & Peimbert 1977; Aller & Czyzak 1979) and *International Ultraviolet Explorer* (*IUE*) UV (Pottasch

et al. 1981) observations of NGC 2371 have been used to estimate an averaged electron temperatures (T_e) in the range 9000–23 000 K, depending on the line ratio used or the adopted electron density (n_e), which is found to be 800–2500 cm^{-3} (e.g. Peña et al. 2001). Kaler, Stanghellini & Shaw (1993) presented the analysis of the optical spectrum in the blue region (∼3700–5000 Å) and showed it to be dominated by the O VI $\lambda\lambda$3811,3834 doublet with contributions from the He II λ4686, C III λ4650, and C IV λ4658. These authors estimated an effective temperature (T_{eff}) for WD 0722+295 of about $T_{eff} = [1–1.2] \times 10^5$ K, consistent with the analysis of *IUE* observations (Pottasch et al. 1981). Since its early classification as a [WR] star of the oxygen sequence (Smith & Aller 1969), its spectral type has swung from early [WC3] (Heap 1982) to [WO1] (Acker & Neiner 2003).

In this work, we intend to unveil the physical structure of the different components of NGC 2371 and to produce an accurate model of its central star. We have obtained Isaac Newton Telescope (INT) spectroscopic observations to study the physical properties (density and temperature) and abundances to describe the ionization structure of the different morphological components of NGC 2371. In conjunction with archival *IUE* observations, the INT spectra are also used to perform a detailed characterization of its CSPN. The paper is organized as follows. In Section 2, we describe the observations used in this work. Section 3 presents the analysis and atmospheric model of WD 0722+295. In Section 4, we present our spectral analysis of NGC 2371 as well as the estimates of the physical structure. In Section 5, we discuss our results and, finally, a summary is presented in Section 6.

2 OBSERVATIONS

Narrow-band images of NGC 2371 were downloaded from the archives of the Canada–France–Hawaii Telescope (CFHT)[1] and *HST* Legacy Archive.[2] The CFHT images were acquired with the multi-object spectrograph (MOS) camera. These images were obtained through the Hα, [O III], and [N II] filters with total exposure times of 1200 s on each filter on 2002 December 18 (Prop. ID.: 02BC17; PI: S. Kwok). The *HST* images were obtained through the F502N, F656N, and F658N filters (hereafter [O III], Hα, and [N II]) on 2007 November 15 with exposure times on each filter of 1600 s (Prop.ID. 11093, PI: K. Noll). A colour-composite image obtained by combining all these optical images is shown in Fig. 1.

Long-slit spectroscopic observations were obtained at the INT of the Observatorio de El Roque de los Muchachos (La Palma, Spain) using the intermediate dispersion spectrograph (IDS) in low- and high-dispersion spectral modes (PI: M. A. Guerrero). The high-resolution spectra were obtained on 2018 October 24 using the EEV10 CCD camera with the R1200U grating. This configuration has a dispersion of 0.48 Å pixel^{-1} over the 3200–4500 Å wavelength range and a plate scale of 0.44 arcsec pixel^{-1}. The low-resolution spectra were acquired on 2018 November 15 using the RED+2 CCD camera with the R400V grating. This configuration has a dispersion of 1.55 Å pixel^{-1} over the 3500–8000 Å wavelength range and a similar plate scale of 0.44 arcsec pixel^{-1}. The slit width was set at 1.1 arcsec in both observing runs. Two slits at PA = 65° (Slit A) and PA = 128° (Slit B) were used with both spectral configurations. Slit B is centred on WD 0722+295, whereas Slit
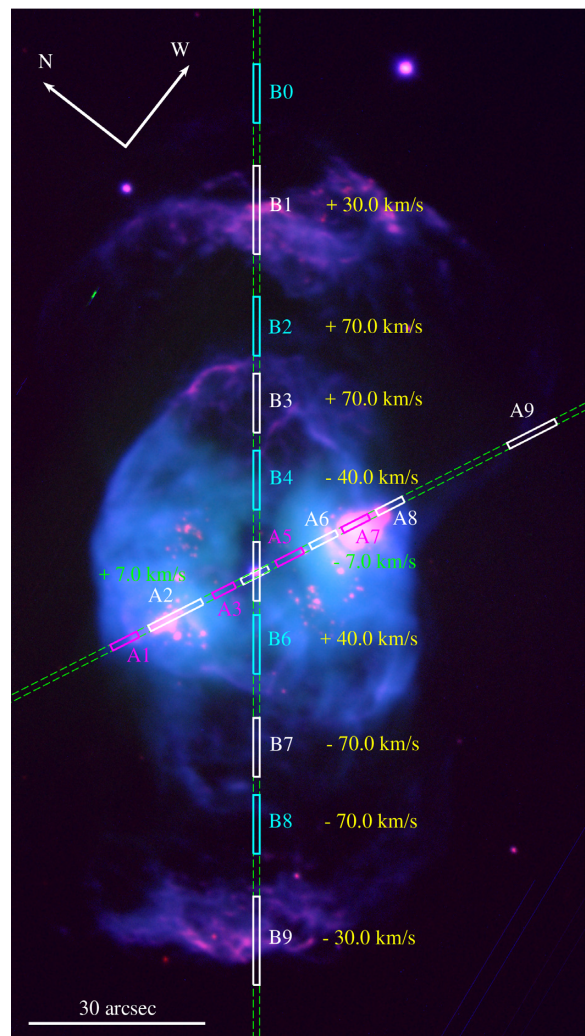
Figure 2. CFHT colour-composite ([O III] – blue, Hα – green, [N II] – red) image of NGC 2371. The (green) dashed line regions represent the slits positions obtained from our INT IDS observations. The PA for the slits are 65° (Slit A – minor axis) and 128° (Slit B – major axis). Different extraction regions are labelled and shown with different colours. The green and yellow velocity measurements correspond to the A2, A7, and B1–B9 extraction regions. See text for details.

A probes the low ionization knots and therefore it does not go exactly across the CSPN. The positions of these slits are overlaid on the colour-composite image of NGC 2371 in Fig. 2. The total integration time on each position and spectral configuration was 900 s. All spectra were analysed following IRAF standard routines. The wavelength calibration was performed using CuAr + CuNe lamps.

In order to study the ionization structure of NGC 2371, we have extracted spectra from different regions defined on each slit using the IRAF task *apall*. Those extracted from Slit A were used to study the central main cavity of NGC 2371 and the dense knots located $\gtrsim$ 16 arcsec from the CSPN, and those from Slit B to study the outermost lobes and different regions of the central cavity along the NW–SE direction. All regions, labelled from A1–A9 to B0–B9, are shown in Fig. 2 and their sizes are indicated in Tables 3 and 4, respectively. We first extracted the 1D spectrum of the CSPN (regions A4 and B5) tracing the stellar continuum along the 2D spectrum. This information was then used as a reference to trace the
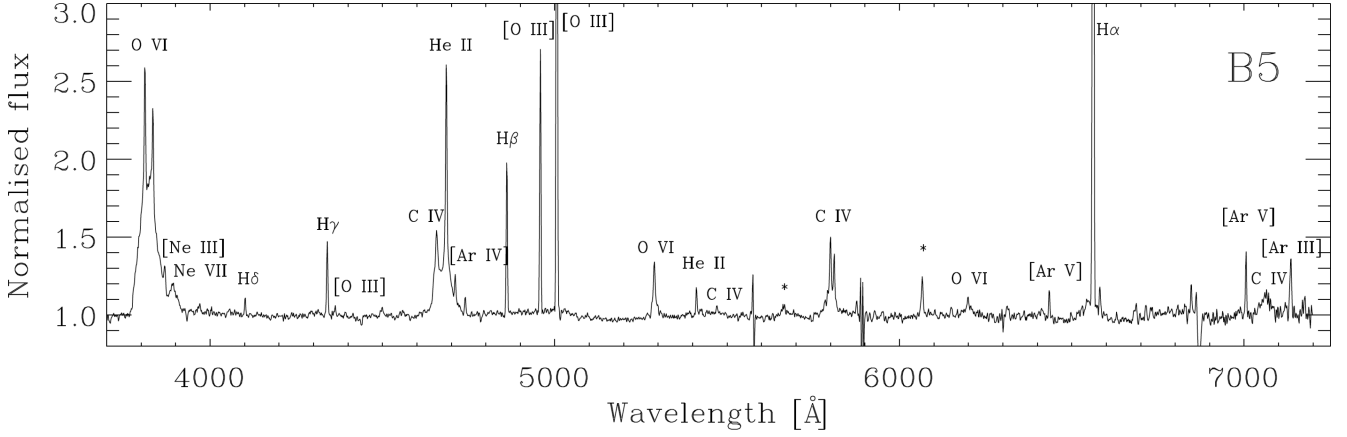
Figure 3. INT IDS low-resolution, normalised spectrum of the CSPN of NGC 2371 obtained from slit B. The most prominent WR features and nebular lines are marked.

Table 1. Parameters for the emission lines considered for the multi-Gaussian fitting of the WR features of the central star in NGC 2371.

ID (1)	(2)	Ion (3)	λ_0 (4)	F (5)	FWHM (6)	EW (7)	λ_c (8)	F/F_{RB} (9)
BB								
1	WR	He II	4686	11.4	28.2	11.2	4686.0	712.5
2	WR	C IV	4658	7.3	15.9	7.0	4656.9	456.3
3	Neb	He II	4686	5.8	4.5	5.7	4685.2	...
4	Neb	Ar IV	4711	0.9	4.5	0.9	4711.5	...
RB								
5	WR	C IV	5801	1.0	7.1	3.1	5799.7	...
6	WR	C IV	5812	0.6	5.4	1.9	5810.5	...
OB								
7	WR	O VI	3820	117.6	57.5	53.2	3818.7	7350.0
8	Neb	O VI	3811	8.0	4.2	3.6	3810.9	...
9	Neb	O VI	3834	5.7	4.1	2.6	3834.0	...
Other								
10	WR	O VI	5290	1.7	9.6	3.2	5288.7	106.3
11	Neb	He II	5412	0.3	3.6	0.7	5411.1	...
12	WR	C IV	5470	0.1	4.6	0.3	5470.4	6.3
13	WR	Ne VII[a]	5666	0.3	8.2	0.8	5664.6	18.8
14	WR	Ne VIII[a]	6068	0.4	6.4	1.6	6066.0	25.0
15	WR	O VI	6200	0.4	18.0	1.4	6200.0	25.0
16	WR	C IV	7060	3.1	30.3	3.5	7062.5	193.8

Notes. (1) Identification number of the Gaussian components in the WR features; (2) Nature of the contributing emission line: WR (broad) or nebular (narrow); (3) Ion responsible for the line; (4) Rest wavelength in Å; (5) Flux in units of 10^{-14} erg cm^{-2} s^{-1}; (6) Full width at half-maximum (FWHM) [Å]; (7) Equivalent width (EW) [Å]; (8) Observed centre of the line; (9) Line fluxes normalized to the RB. The ratio has been computed adopting a $F(\mathrm{RB}) = 100$.
[a]This identification is discussed in Section 5.

nebular spectra (regions A1–A3, A5–A9, B0–B4, and B6–B9) along the 2D spectra, as these regions do not show continuum emission. Since Slit A misses some stellar flux, the spectrum extracted for region A4 has not been used for stellar modelling. Finally, we note that all extracted spectra were corrected for extinction by using the $c(\mathrm{H}\beta)$ value estimated from the Balmer decrement method. We assume intrinsic Balmer decrement ratio corresponding to a case B photoionized nebula of $T_e = 10\,000$ K and $n_e = 100$ cm^{-3} (see Osterbrock & Ferland 2006) and the reddening curve of Cardelli, Clayton & Mathis (1989).

3 WD 0722+295 – THE CSPN OF NGC 2371

The optical spectrum of WD 0722+295 obtained from our INT IDS observations is presented in Fig. 3. The stellar spectrum exhibits the classic WR blue and red bumps (BB and RB) at ∼4686 and ∼5806 Å, respectively, as well as a broad O VI feature at ∼3820 Å (see also fig. 1 in Kaler et al. 1993). Other emission lines related to WR features such as those reported in Acker & Neiner (2003) – namely, O VI 5290 Å, C IV 5470 Å and 7060 Å, and He II 5412 Å – are also present in the optical spectrum. Furthermore, we also detect the O VI 6200 Å as a broad emission line. All identified WR features as well as some contributing nebular lines are marked in Fig. 3. We note the presence of narrow emission lines at ≈5665 and ≈6066 Å marked with an asterisk in Figs 3 and 4. There has been controversy in the identification of these lines, which can be assigned either to the O VII λ5666 and O VIII λ6068 lines or to the Ne VII λ5666 and Ne VIII λ6068 lines. This is discussed in Section 5.

To provide an appropriate description of the spectrum and spectral classification of WD 0722+295, the contribution from nebular lines blended with the broad WR features needs to be accounted for. This was done by applying the analysis described by Gómez-González et al. (2020). This method consists on fitting the broad WR features with multi-Gaussian components using a tailor-made code that uses the IDL routine LMFIT.[3] As a result, fluxes, central wavelength, full width at half-maximum (FWHM), and equivalent widths (EW) from the WR spectral features as well as contributing nebular lines have been estimated. All these parameters are listed in Table 1. We note that those lines listed as WR features have FWHM larger than those of the nebular narrow lines, that is, FWHM > 4.5 Å.

Fig. 4 shows the fits to the different WR features of the WD 0722+295. Two of these bumps are composed of several blended emission lines and need a careful modelling in order to separate their broad and narrow contributions. The O-bump feature is made of a broad O VI (FWHM of 57.5 Å), two O VI narrow lines (FWHM <4.5 Å), and several Ne lines at the red wing (see Table 1). It is clear that the broad O VI 3820 Å has a stellar origin and, although the other two O VI lines have FWHM that suggest a nebular origin, some contribution from the star is expected according to our stellar

---

[3]The LMFIT function (lmfit.pro) performs a non-linear least-squares fit to a function with an arbitrary number of parameters. It uses the Levenberg–Marquardt algorithm, incorporated in the routine *mrqmin* from Press et al. (1992).
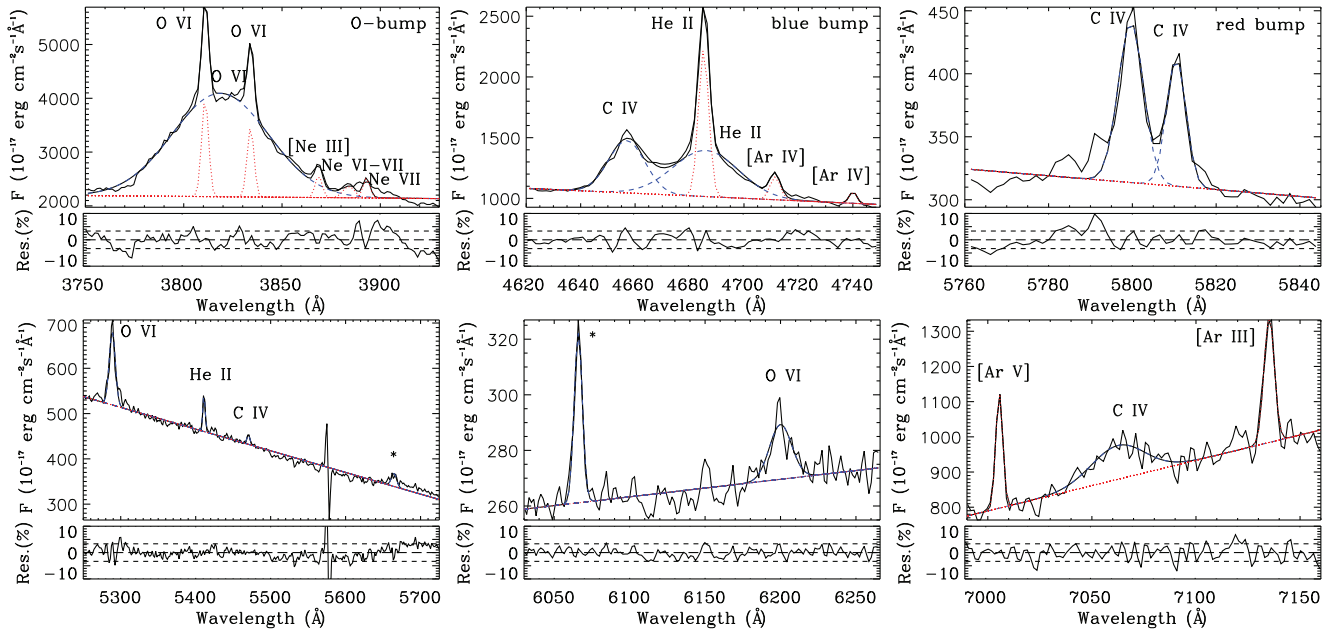
Figure 4. Multicomponent Gaussian fits to the O-bump (*top left*), blue bump (*top centre*), and red bump (*top right*) panels. The bottom panels show other WR features in the spectrum of WD 0722+295. The (blue) dashed lines represent the fits to the broad (stellar) features, the (red) dotted line the fits to the nebular emission, and the (black) line the sum. Residuals are shown at the bottom of each panel.

atmosphere model (see Section 3.1 and Fig. 5). The Gaussian-fitting method shows that the O VI lines at 3811 and 3834 Å contribute about 10 per cent to the O-bump. Thus, this can be considered as an upper limit to the nebular contribution. Other narrow emission lines also contribute to the BB. For example, the He II, which is blended with WR features contributes $\simeq$30 per cent of the total flux of the BB (He II 4686 Å + C IV 4658 Å; see Table 2). There is no contribution of nebular lines to the RB (C IV 5801 Å + C IV 5812 Å).

With reliable flux estimates for each WR feature, we can assess the spectral classification of WD 0722+295. For this, we estimated the line ratios of oxygen, carbon, and helium WR features relative to the RB (column 9 of Table 1) and compared them to those defining the quantitative classification scheme of [WR] stars listed in table 2 of Acker & Neiner (2003). According to this scheme, WD 0722+295 fulfils the criteria for a [WO1]-type star, but we note that the FWHM of the RB is around half of that suggested for this spectral type. One could argue that using dereddened flux ratios is model dependent and less accurate than using EW ratios. For this, we also compared our results listed in Table 1 with the classification scheme proposed in Crowther et al. (1998) and found that the EW ratio of the O VI 3820 Å WR feature over the RB is 73.5, above the limit of ~1.6 suggested by these authors for a [WO1] spectral type.

3.1 NLTE analysis of WD 0722+295

To obtain a more quantitative description of the properties of WD 0722+295, we have analysed optical and UV spectra by means of the updated version of the Potsdam WR (POWR)[4] NLTE stellar atmosphere code (Gräfener, Koesterke & Hamann 2002; Hamann & Gräfener 2004). Details of the computing scheme can be found in Todt et al. (2015) and the most recent example of
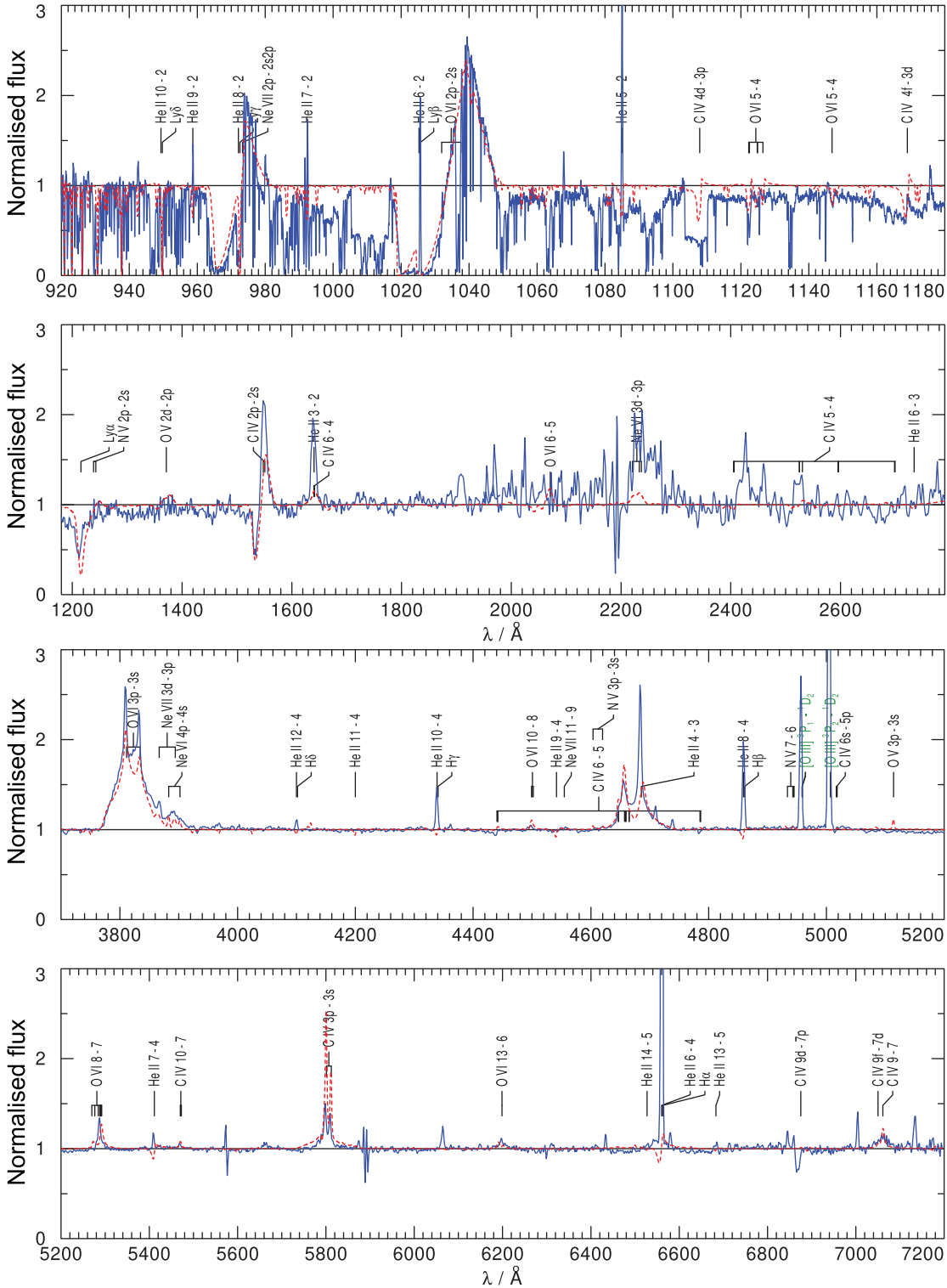
the capabilities of the POWR code performed by our group can be found in Toalá et al. (2019) for the case of the [WR]-type CSPN of NGC 40.

Available UV *Far Ultraviolet Spectroscopic Explorer* (*FUSE*) and *IUE* observations of WD 0722+295 were retrieved from the Mikulski Archive for Space Telescopes.[5] The UV observations were analysed in conjunction with the optical INT IDS spectra with the POWR stellar atmosphere code. The *FUSE* observations correspond to Obs. ID. p1330301000 (PI: L. Bianchi) and were obtained on 2000 February 26 with the LWRS aperture for a total exposure time of 5259 s. The *IUE* data, taken on 1979 April 7, correspond to the Obs. ID. SWP04883 and LRW04210 (Program ID SP127; PI: S. R. Pottasch) with exposure times of 1560 and 2700 s, respectively. The spectra imply a reddening of $E(B - V) = 0.08$ mag using the Cardelli extinction law which is consistent with the value estimated by Herald & Bianchi (2004).

The parameters of our best-fitting model are listed in Table 2. We note that the stellar mass was adopted to be $M_\star = 0.6\ M_\odot$, a typical value for CSPNe (e.g. Miller Bertolami 2016, and references therein). The resultant temperature, defined at $\tau_{\rm Ross} = 20$, which is constrained by the relative strength of the emission lines, is $T_{\rm eff} = 130$ kK. A luminosity of $L_\star = 2820\ L_\odot$ is estimated by using a distance $d = 1.75$ kpc (Bailer-Jones et al. 2018) and the resultant mass-loss rate is $\dot{M} = 1.78 \times 10^{-8}\ M_\odot$ yr^{-1}. We note that the estimated value for the mass-loss rate is somewhat smaller than those listed for other [WR] stars in Todt et al. (2013b), who used a canonical luminosity of $L = 5000\ L_\odot$ to calculate the mass-loss rates from the $R_{\rm t}$ values obtained from the analysis. Taking the lower luminosity of NGC 2371 into account, our value of $\dot{M}$ is comparable with the one derived for Hen 2-55. Furthermore, our $R_{\rm t} = 20\ R_\odot$ is fully compatible with the value of $R_{\rm t} = 15^{+10}_{-5}\ R_\odot$ by Herald & Bianchi (2004). They used the same luminosity as in

[4]http://www.astro.physik.uni-potsdam.de/~wrh/PoWR

[5]https://archive.stsci.edu/hst/

Figure 5. Comparison between our POWR model (red dashed line) with optical and UV observations (blue solid line).

our analysis (based on the distance of $d = 1.5$ kpc), but assumed a smooth wind with $D = 1$, where we adopted a density contrast of $D = 10$ for a clumped wind. Therefore, their mass-loss rate is about a factor $\sqrt{10}$ larger than ours.

Our best-fitting model to the P Cygni profiles in the UV spectra resulted in a stellar wind velocity $v_\infty = 3700$ km s^{-1} with a

micro-turbulence of less than 3 per cent. The micro-clumping parameter D, which is defined as the density contrast between a smooth wind and a clumpy wind, is estimated to be 10. Fig. 5 shows a comparison between the POWR model of WD 0722+295 and the optical and UV spectra, and Fig. 6 presents the synthetic spectral energy distribution (SED) from the far-UV to the infrared

Table 2. Parameters of WD 0722+295 obtained with POWR.

Parameter	Value	Comment
$T_{\rm eff}$ (kK)	130	Defined at $\tau_{\rm Ross} = 20$
d (kpc)	1.75	Bailer-Jones et al. (2018)
$\log(L_\star/L_\odot)$	3.45	
$R_\star$ ($R_\odot$)	0.105	
$R_{\rm t}$ ($R_\odot$)	20	
D	10	Density contrast
$\log(\dot{M}/{\rm M_\odot\,yr^{-1}})$	-7.75	for $D = 10$
v_∞ (km s^{-1})	3700	
$M_\star$ (M$_\odot$)	0.6	Stellar mass adopted
Chemical abundances (mass fraction)		
He	0.71	
C	0.20	
N	0.001	
O	0.06	
Ne	0.03	
Fe	1.4×10^{-3}	

(IR) in comparison with UV and optical spectra and IR photometry obtained from public archives.

The abundances for WD 0722+295 derived from our best-fitting model are also listed in Table 2. Whereas the stellar parameters agree with those reported by Herald & Bianchi (2004, see their table 6), our abundance determinations are at variance, with our He abundance 30 per cent larger and our N/O ratio half their value. The differences can be attributed to the use of different stellar atmosphere codes, as Herald & Bianchi (2004) use a relatively old version of the CMFGEN code (Hillier & Miller 1998, 1999), but we note that our abundance determination is improved by the simultaneous modelling of high-quality optical spectra and UV data.

4 PHYSICAL CONDITIONS, EXCITATION, AND CHEMICAL ABUNDANCES OF NGC 2371

Examples of INT IDS spectra extracted from Slits A and B are shown in Fig. 7. The complete list of lines detected in the different extraction regions and their dereddened intensities relative to an arbitrary value 100 for Hβ are presented in Tables 3 and 4. The spectra extracted from Slit B, particularly those from regions B2, B3, B7, and B8, show fewer emission lines than those extracted from Slit A, in agreement with the lower surface brightness of the major axis probed by Slit B (see Fig. 1). Intensity uncertainties at 1σ are provided in these tables, together with the values derived for c(Hβ) and the corresponding fluxes of the Hβ line for each extraction region.

Different line intensity ratios have been used to determine the physical conditions of the different regions in NGC 2371 using the IRAF task *temden* (Tody 1993). T_e was estimated using the [O III] emission lines for most regions and the [N II] emission lines whenever possible, i.e. in regions A2, A7, and A8. n_e was derived using the [S II] $\lambda\lambda6717,6731$, [Cl III] $\lambda\lambda5517,5537$, and [Ar IV] $\lambda\lambda4711,4740$ doublets whenever available. The values of T_e and n_e, together with their 1σ uncertainties are listed in the bottom rows of Tables 3 and 4.

The values of T_e([O III]) listed in Tables 3 and 4 reveal notable temperature gradients in the central cavity of NGC 2371. The innermost regions A2, A3, A5, A5, B4, and B6 immediately around the CSPN show consistently high values of T_e([O III]) in the range 18 000–19 000 K, that decrease to $\approx$15 000–16 000 K in

the outermost regions A1 and A8, and have the notably lowest value of $\approx$13 800 K in the region A7, which probes the SW knot.

Such high values of T_e in the close vicinity of the CSPN of NGC 2371 arise from its 130 kK high $T_{\rm eff}$ (see Section 3.1). Interestingly, T_e([N II]) is only computed on regions that probe the NE and SW knots. The much lower values of T_e([N II]) in these regions with respect to those of T_e([O III]) indicate that these apertures probe a mix of low- and high-excitation material.

As for n_e([S II]), it varies in Tables 3 and 4 from 100 to 1640 cm^{-3}, with the densest region corresponding to the core of the SW knot A7, whose head A6 and tail A8 have intermediate density values 600–700 cm^{-3}. The NE knot seems to have lower density estimates than the SW know, but we note that Slit A does not go exactly across the NE knot. Furthermore, the NE knot is smaller and appears more fragmented than the SW knot (see Fig. 1, right-hand panels). These facts will have consequences for the abundance determination too (see below).

Whereas the regions A3, A5, B4, and B6 immediately around the CSPN share similar values of T_e, the densities n_e([S II]) are larger for regions B4 and B6 ($n_e = 810$–1100 cm^{-3}) than for regions A3 and A5 (100–280 cm^{-3}). The latter seem to probe a hollow region around the CSPN. Regions B1 and B9 extracted from the outer edges of the major axis of NGC 2371 have the lowest temperature values (T_e([O III])$\simeq$11 800–13 100 K), but they have higher densities (n_e([S II]) $\approx$ 400 cm^{-3}) than regions within the inner main cavity.

In order to unveil differences in excitation from different morphological features in NGC 2371, we plot in Fig. 8 line ratios of key emission lines derived from the INT IDS spectroscopy (see Akras & Gonçalves 2016, and references therein), including [N II] 6583/Hα versus [O III] 5007/Hα (top panel) and [S II] (6717 + 6731)/Hα versus [O III] 5007/Hα (bottom panel). Differences in excitation are clear: regions close to the star (inner regions – A3, A5, B4, B5, B6) show the lowest [O III]/Hα and [N II]/Hα line ratios, whereas other regions, particularly the outermost regions B1 and B9, and the regions A7 and A8 of the SW knot show the highest [O III]/Hα and [N II]/Hα.

In Figure 8 bottom panel, we show the theoretical limit between photoionized and shocked material log([O III]/Hα) = 1.89 log([S II]/Hα) + 2.46, as estimated by Danehkar et al. (2018) based on the models presented by Raga et al. (2008). Line ratios below this limit show gas excited by ionization, while regions above present shocked excited gas. Most morphological features in NGC 2371 are located below this theoretical limit, i.e. they are excited by photoionization. On the other hand, the outermost B1 and B9 regions are located above the dashed line, suggesting that they are excited by shocks as could be expected if these structures were expanding at high speed into the interstellar medium (ISM). The spectra of regions A7 and A8 extracted from the head of the SW dense knot also present line intensity ratios typical of shock excitation.

The *HST* WFC3 images of NGC 2371 have also been used to provide a complementary view of its ionization structure. Ratio maps were obtained by dividing the [O III], [N II], and [S II] calibrated images by the Hα image (see Fig. 9). We note that the *HST* [S II] image does not have adequate signal-to-noise ratio in the NW and SE lobes of NGC 2371. Thus, the line ratio calculations were only performed for the innermost regions of NGC 2371. We defined four different rectangular regions (see Fig. 9 left-hand panel) to study the dominant excitation mechanisms: a large region that includes most of the main inner cavity of NGC 2371, two regions covering
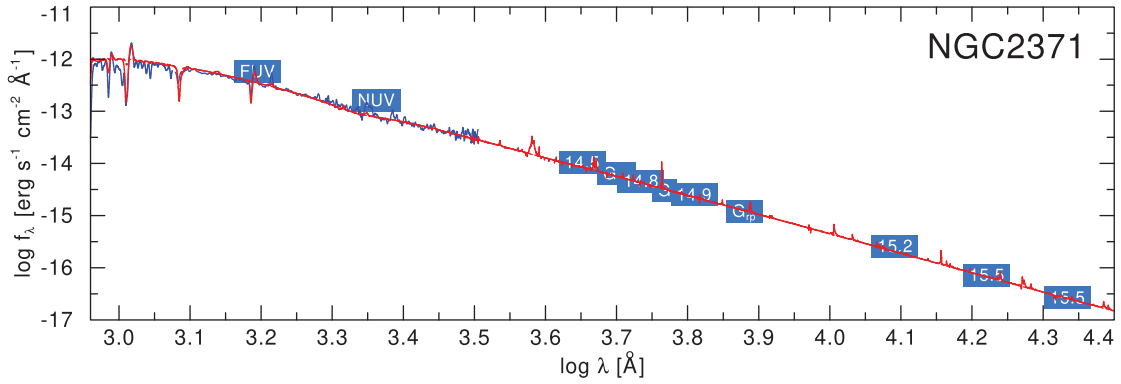
Figure 6. Comparison between our POWR model (red line) with observed spectra in the optical and UV and IR photometry (blue).
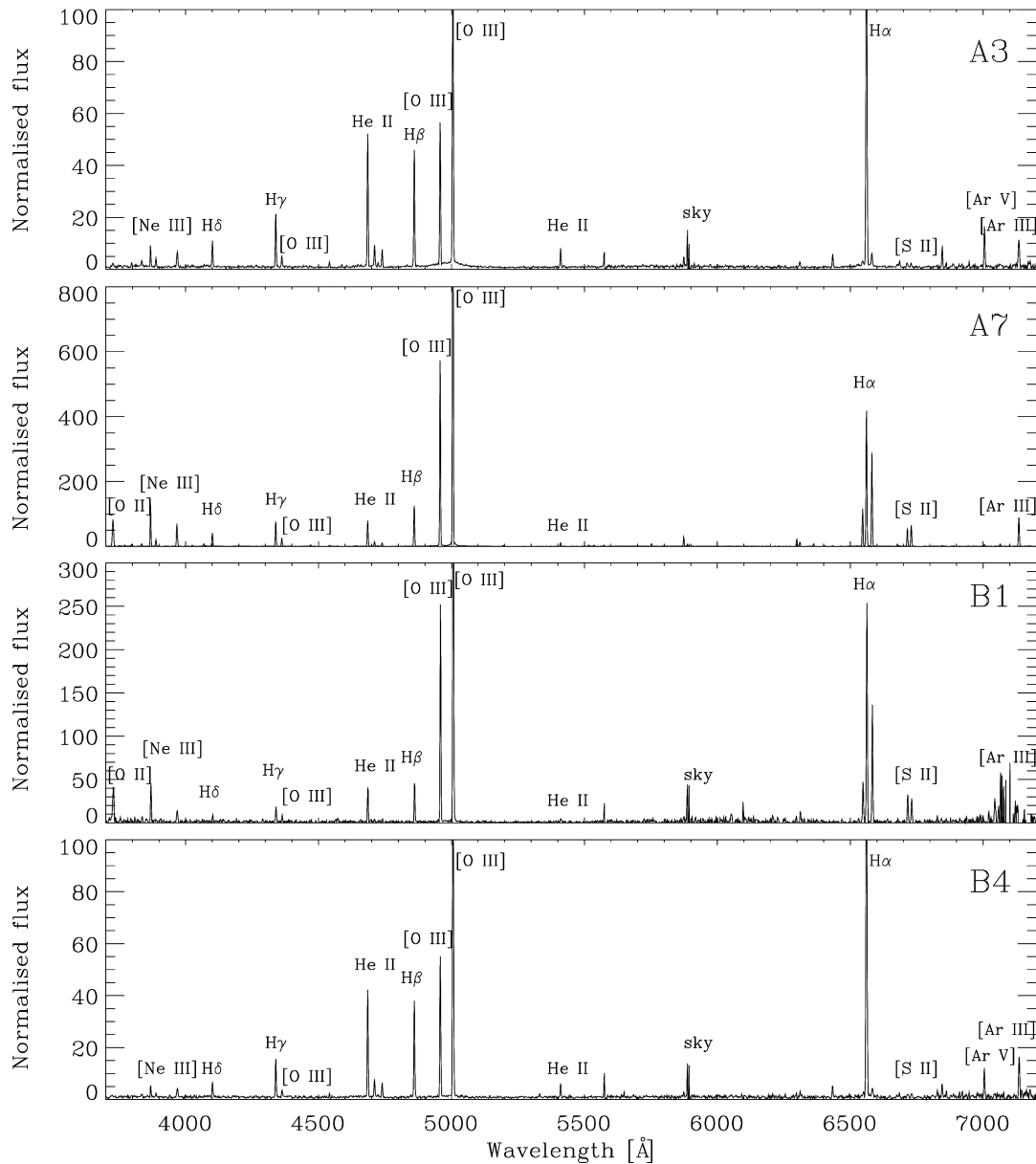
Figure 7. Examples of INT IDS spectra of NGC 2371. The panels show the spectra extracted from regions A3, A7, B1, and B4. The most prominent lines are labelled. See Tables 3 and 4 for details on the fluxes.

Table 3. Reddening-corrected line intensities for selected regions of Slit A of NGC 2371.

λ_0	Line	A1 (5 arcsec)	A2 (10 arcsec)	A3 (4 arcsec)	A5 (5 arcsec)	A6 (5 arcsec)	A7 (5 arcsec)	A8 (5 arcsec)	A9 (10 arcsec)
3726.2	[O II]	33.2 ± 5.4	35.3 ± 1.8	11.6 ± 2.4	16.5 ± 3.0	24.1 ± 1.7	201.2 ± 4.9	141.7 ± 8.1	...
3797.9	H θ	8.4 ± 3.2	6.5 ± 0.7	6.9 ± 1.7	7.2 ± 1.5	5.7 ± 0.6	8.6 ± 0.8	...	...
3835.4	H η	13.5 ± 3.9	9.6 ± 0.8	12.3 ± 2.1	12.2 ± 1.8	9.9 ± 0.6	9.3 ± 0.7	...	...
3868.8	[Ne III]	99.4 ± 7.0	81.3 ± 1.9	32.6 ± 2.2	33.5 ± 2.2	74.7 ± 1.2	157.4 ± 2.3	97.5 ± 6.1	...
3889.1	H ζ	16.5 ± 3.5	16.0 ± 0.9	12.6 ± 1.7	14.9 ± 1.5	16.2 ± 0.6	21.9 ± 0.8	15.6 ± 2.7	...
3967.5	[Ne III]	49.8 ± 5.0	44.3 ± 1.4	24.4 ± 2.2	29.5 ± 2.0	43.7 ± 1.0	72.1 ± 1.4	46.1 ± 3.7	...
3970.0	H ε	...	...	...	...	...	...	...	...
4026.2	He I	4.6 ± 2.6	2.0 ± 0.4	1.2 ± 0.8	2.7 ± 1.1	2.2 ± 0.4	2.6 ± 0.3	1.1 ± 0.9	...
4068.6	[S II]	2.3 ± 1.5	2.8 ± 0.5	2.2 ± 1.0	...	...	...	...	...
4101.7	H δ	31.9 ± 3.4	32.7 ± 1.0	27.2 ± 1.8	31.9 ± 1.5	34.1 ± 0.8	33.3 ± 0.7	26.5 ± 2.4	...
4200.0	He II	...	...	...	...	2.3 ± 0.2	1.2 ± 0.2	...	...
4340.5	H γ	54.0 ± 3.5	57.2 ± 1.0	49.9 ± 1.8	54.9 ± 1.6	56.6 ± 1.0	57.4 ± 0.9	46.2 ± 3.3	...
4363.2	[O III]	19.6 ± 2.2	17.1 ± 0.6	10.0 ± 1.0	9.7 ± 0.8	17.0 ± 0.6	18.3 ± 0.4	16.0 ± 1.8	...
4471.5	He I	...	...	...	...	...	3.7 ± 0.2	3.8 ± 1.1	...
4540.0	He II	3.8 ± 1.1	4.3 ± 0.4	3.4 ± 0.8	4.1 ± 0.7	4.4 ± 0.5	2.4 ± 0.3	2.4 ± 0.8	...
4686.0	He II	112.8 ± 3.6	116.4 ± 1.6	122.8 ± 2.9	133.0 ± 2.5	118.5 ± 1.4	65.2 ± 0.9	78.0 ± 2.9	...
4711.4	[Ar IV]	22.6 ± 1.8	24.2 ± 0.6	20.9 ± 1.3	20.4 ± 1.0	25.2 ± 0.6	11.2 ± 0.4	14.5 ± 1.4	...
4740.2	[Ar IV]	14.5 ± 1.4	17.7 ± 0.6	14.8 ± 1.1	14.5 ± 0.9	18.5 ± 0.6	8.1 ± 0.4	10.3 ± 1.2	...
4861.4	H β	100 ± 2.2	100 ± 0.9	100 ± 1.8	100 ± 1.6	100 ± 0.7	100 ± 0.5	100 ± 2.6	100 ±
4958.9	[O III]	305.2 ± 2.2	213.6 ± 8.1	122.4 ± 1.0	118.7 ± 0.6	210.4 ± 9.3	392.3 ± 11.9	283.1 ± 27.2	453.1 ± 152.8
5006.8	[O III]	907.0 ± 5.7	638.5 ± 5.7	366.5 ± 2.6	354.2 ± 1.5	628.5 ± 6.8	1174.7 ± 8.6	849.4 ± 27.9	1130.4 ± 419.3
5197.9	[N I]	...	...	...	...	...	1.8 ± 0.1	1.1 ± 0.3	...
5411.0	He II	6.2 ± 0.7	8.1 ± 0.2	7.4 ± 0.5	8.1 ± 0.4	8.3 ± 0.2	4.6 ± 0.1	4.6 ± 0.6	...
5517.7	[Cl III]	...	1.0 ± 0.1	...	...	1.0 ± 0.1	1.4 ± 0.1	...	...
5537.9	[Cl III]	...	0.7 ± 0.1	...	...	0.8 ± 0.1	1.1 ± 0.1	...	...
5754.6	[N II]	...	0.4 ± 0.1	...	...	...	2.3 ± 0.1	2.2 ± 0.6	...
5875.6	He I	0.9 ± 0.2	2.0 ± 0.1	1.7 ± 0.2	1.7 ± 0.2	1.8 ± 0.1	6.8 ± 0.2	4.3 ± 0.6	...
6101.0	[K IV]	...	0.5 ± 0.1	...	...	0.7 ± 0.1	0.2 ± 0.1	0.6 ± 0.4	...
6234.0	He II	...	...	...	...	...	...	...	...
6312.1	[S III]	3.8 ± 0.4	...	2.1 ± 0.4	1.9 ± 0.3	4.2 ± 0.1	5.6 ± 0.1	3.9 ± 0.7	...
6363.0	[O I]	...	0.4 ± 0.1	...	...	...	3.3 ± 0.1	1.8 ± 0.5	...
6406.0	He II	...	1.1 ± 0.2	...	1.0 ± 0.5	1.2 ± 0.2	0.5 ± 0.2	...	...
6435.1	[Ar V]	2.1 ± 0.6	3.8 ± 0.3	5.6 ± 0.7	6.7 ± 0.6	4.0 ± 0.2	0.9 ± 0.1	1.9 ± 0.9	...
6548.1	[N II]	4.5 ± 0.2	8.3 ± 0.1	2.8 ± 0.1	1.8 ± 0.0	4.4 ± 0.1	66.2 ± 1.1	52.0 ± 3.4	...
6562.8	H α	287.0 ± 5.5	287.0 ± 1.6	287.0 ± 4.1	287.0 ± 3.1	287.0 ± 1.4	287.0 ± 1.5	286.5 ± 6.4	248.5 ± 64.3
6583.5	[N II]	15.8 ± 1.3	25.0 ± 0.5	7.9 ± 0.7	6.0 ± 0.4	15.3 ± 0.3	191.6 ± 1.2	149.9 ± 4.5	...
6678.2	He I	...	...	...	...	...	4.5 ± 0.3	2.4 ± 0.9	...
6716.5	[S II]	8.0 ± 1.6	7.9 ± 0.4	3.3 ± 1.0	2.2 ± 0.8	6.1 ± 0.3	46.0 ± 0.8	51.7 ± 3.3	...
6730.8	[S II]	6.6 ± 1.5	8.2 ± 0.4	2.5 ± 0.9	1.8 ± 0.9	5.9 ± 0.3	58.2 ± 0.9	50.4 ± 3.2	...
7005.9	[Ar V]	15.6 ± 4.0	25.6 ± 1.3	41.9 ± 4.0	43.6 ± 3.2	29.0 ± 1.0	7.5 ± 0.5	15.4 ± 4.5	...
7065.2	He I	...	2.3 ± 0.6	...	...	2.8 ± 0.5	9.2 ± 0.5	...	...
7135.8	[Ar III]	78.7 ± 6.6	84.2 ± 1.7	40.0 ± 3.7	30.0 ± 2.4	75.8 ± 1.3	158.2 ± 1.7	99.0 ± 9.1	...
log(H β)	(erg cm^{-2} s^{-1})	−13.26	−12.55	−13.45	−13.14	−12.68	−12.73	−13.65	−15.24
c(H β)		0.38	0.16	0.06	0.22	0.17	0.08	0	...
A_V	(mag)	0.80	0.32	0.13	0.47	0.35	0.16	0	0
T_e([O III])	(K)	16 000 ± 800	17 800 ± 200	18 000 ± 900	18 000 ± 800	18 000 ± 200	13 800 ± 100	15 000 ± 500	...
T_e([N II])	(K)	...	11 000 ± 1100	...	...	...	9330 ± 120	10 300 ± 1100	...
n_e ([S II])	(cm^{-3})	250 ± 60	850 ± 50	100 ± 80	280 ± 200	680 ± 40	1640 ± 40	620 ± 50	...
n_e ([Cl III])	(cm^{-3})	...	...	...	...	270 ± 220	880 ± 80	...	...
n_e ([Ar IV])	(cm^{-3})	...	420 ± 80	...	50 ± 170	440 ± 90	330 ± 130	100 ± 180	...

the SW and NE dense knots, and a region that includes only gas around the central star. We computed the pixel-by-pixel line ratios and these are plotted in Fig. 8 as colour-coded regions alongside the results found for regions extracted from Slits A and B. The results are consistent with those obtained from the spectroscopic observations.

Finally, the abundances were computed using the extensively tested code PYNEB developed by Luridiana, Morisset & Shaw (2015). PYNEB computes the physical conditions (T_e and n_e) and ionic and total abundances. Ionic abundances were calculated with their corresponding temperature and averaged density based on the ionization potential (IP) of the ion. We note that the T_e and n_e

values obtained from PYNEB (not presented here) are consistent within <2 per cent with those listed in Tables 3 and 4 obtained in IRAF. For the calculation of ionic abundances, we only considered emission lines with uncertainties smaller than 50 per cent, resulting in abundances with typical uncertainties of a few per cent. The total abundances of He, O, N, Ne, Ar, S, and Cl, listed in Table 5 for apertures A1–A3 and A5–A8, were computed adopting the ionization correction factors (ICFs) provided by Delgado-Inglada, Morisset & Stasińska (2014). The error budget of the abundances of heavy elements in Table 5 is mostly dominated by uncertainties in the computation of those ICFs, which are notably large for high excitation nebulae.

Table 4. Reddeding-corrected line intensities for selected regions of Slit B of NGC 2371.

λ_0	Line	B1 (15 arcsec)	B2 (10 arcsec)	B3 (10 arcsec)	B4 (10 arcsec)	B5 (10 arcsec)	B6 (10 arcsec)	B7 (10 arcsec)	B8 (10 arcsec)	B9 (15 arcsec)
3726.2	[O II]	258.7 ± 41.7	...	...	...	...	...	...	...	145.9 ± 32.4
3868.8	[Ne III]	190.1 ± 35.2	100.6 ± 37.2	100.1 ± 29.5	36.8 ± 3.8	...	41.4 ± 2.6	...	...	175.8 ± 35.9
3888.7	He I	...	...	...	12.2 ± 3.1	...	14.1 ± 2.0	...	...	...
3967.5	[Ne III]	73.9 ± 18.9	...	...	29.8 ± 3.7	...	27.9 ± 2.3	...	...	73.3 ± 21.6
4101.7	H δ	31.4 ± 11.6	...	...	30.7 ± 3.0	26.6 ± 2.4	34.2 ± 2.1	38.4 ± 13.7	...	30.2 ± 11.6
4340.5	H γ	53.0 ± 10.8	57.9 ± 18.7	36.9 ± 12.3	56.5 ± 3.2	90.0 ± 2.9	58.5 ± 2.0	51.5 ± 14.3	72.5 ± 23.4	55.7 ± 10.7
4363.2	[O III]	21.6 ± 7.7	44.5 ± 17.1	...	11.7 ± 2.0	10.6 ± 3.1	12.0 ± 1.2	...	...	14.4 ± 6.5
4540.0	He II	...	...	...	...	...	3.8 ± 0.8	...	...	...
4686.0	He II	96.9 ± 13.3	107.6 ± 19.9	107.6 ± 15.4	130.8 ± 4.0	...	133.1 ± 3.2	126.1 ± 12.0	138.4 ± 22.7	103.3 ± 12.9
4711.4	[Ar IV]	...	...	15.4 ± 8.6	22.4 ± 2.0	...	20.9 ± 1.1	...	...	...
4740.2	[Ar IV]	...	...	12.6 ± 7.9	16.1 ± 1.7	14.6 ± 1.6	17.3 ± 0.9	...	...	...
4861.4	H β	100 ± 9.6	100 ± 16.9	100 ± 12.2	100 ± 3.4	100 ± 1.3	100 ± 1.8	100 ± 8.8	100 ± 15.6	100 ± 10.6
4958.9	[O III]	533.3 ± 21.2	407.2 ± 28.1	278.2 ± 17.7	135.7 ± 3.8	154.7 ± 1.9	135.1 ± 2.1	253.5 ± 12.5	329.5 ± 23.5	478.5 ± 22.3
5006.8	[O III]	1549.7 ± 31.1	1191.3 ± 45.1	807.0 ± 26.0	401.9 ± 6.0	448.3 ± 3.1	394.9 ± 3.4	711.3 ± 21.5	954.6 ± 41.3	1385.8 ± 38.6
5411.0	He II	5.7 ± 2.2	...	...	6.5 ± 0.6	8.1 ± 0.9	7.5 ± 0.4	7.4 ± 2.5	...	5.3 ± 2.1
5875.6	He I	...	...	...	2.0 ± 0.4	...	2.1 ± 0.2	...	...	...
6101.0	[K IV]	...	...	...	...	...	...	...	...	...
6312.1	[S III]	5.8 ± 2.9	...	...	1.7 ± 0.6	...	2.0 ± 0.3	...	...	4.8 ± 1.9
6435.1	[Ar V]	...	...	...	4.3 ± 0.9	3.8 ± 1.7	4.2 ± 0.4	...	...	...
6548.1	[N II]	46.0 ± 6.3	24.5 ± 11.1	18.2 ± 2.8	3.4 ± 0.2	...	1.0 ± 0.1	...	...	31.8 ± 5.1
6562.8	H α	287.0 ± 17.7	287.0 ± 26.3	287.0 ± 17.4	287.0 ± 6.8	287.0 ± 3.9	287.0 ± 4.3	287.0 ± 17.6	287.0 ± 32.2	287.0 ± 15.0
6583.5	[N II]	159.0 ± 13.0	49.3 ± 11.7	43.0 ± 7.0	6.2 ± 1.3	12.5 ± 2.7	3.7 ± 0.5	9.4 ± 4.1	21.0 ± 10.0	106.6 ± 9.0
6716.5	[S II]	46.6 ± 9.9	...	17.4 ± 7.9	2.8 ± 1.6	2.5 ± 1.8	2.0 ± 0.6	...	...	33.6 ± 6.6
6730.8	[S II]	41.4 ± 9.4	...	18.0 ± 8.2	2.8 ± 1.5	2.9 ± 2.3	2.2 ± 0.6	...	...	31.1 ± 6.5
7005.9	[Ar V]	...	...	...	28.0 ± 5.1	23.1 ± 4.8	27.8 ± 2.8	...	...	...
7135.8	[Ar III]	115.7 ± 2.1	127.3 ± 55.3	62.5 ± 28.4	49.5 ± 5.9	37.3 ± 5.9	28.1 ± 2.6	50.0 ± 17.8	...	98.9 ± 22.5
$\log(H \beta)$	(erg cm^{-2} s^{-1})	-13.38	-14.10	-13.87	-13.13	-12.88	-12.66	-13.67	-14.14	-13.43
$c(H \beta)$		0.49	0.41	0.46	0.35	0.56	0.54	0.54	0.44	0.47
A_V	(mag)	1.02	0.86	0.98	0.74	1.17	1.14	1.13	0.91	0.99
$T_e([O III])$	(K)	$13\,100 \pm 1700$	$22\,000 \pm 5000$	...	$18\,600 \pm 1600$	$15\,100 \pm 2300$	$19\,000 \pm 1000$	...	...	$11\,800 \pm 1800$
$n_e([S II])$	(cm^{-3})	380 ± 30	...	690:	810 ± 360	1190 ± 240	1070 ± 30	...	...	450 ± 30
$n_e ([Ar IV])$	(cm^{-3})	...	...	1600 ± 500	140 ± 200	...	2160 ± 40	...	...	...

5 DISCUSSION

NGC 2371 has a multicomponent morphology with (1) a pair of outer lobes aligned along PA = 128°, (2) a high-excitation main shell with apparent elliptical morphology aligned along the same direction with two lower excitation caps at its tips, and (3) two ensembles of dense low ionization knots in the equatorial region of the main shell, although misaligned with the previous structures. We provide next a description of the overall physical structure of NGC 2371 using kinematical information to help us interpret its different components.

### 5.1 On the kinematic structure of NGC 2371

By Gaussian fitting of bright emission lines, their centroid can be routinely determined with an accuracy ∼10 times better than the spectral resolution, which is ∼200 km s^{-1} for our observations with the R400V grating and ∼70 km s^{-1} for those with the R1200U grating. Thus, our low-resolution spectra allow us to investigate the kinematics of structures that have velocities ≥20 km s^{-1}. This is illustrated in Fig. 10, which presents three sections of the R400V 2D spectrum obtained with the Slit B along the major nebular axis. These spectral sections include the H α + [N II], [O II], and [O III] emission lines. Velocity gradients are clearly seen in these (as well as other) spectral lines as an S-shaped pattern in the position–velocity (PV) map along the nebular axis, but tilted along the opposite direction for the main cavity.

These PV maps have been used to estimate the systemic radial velocities of the different morphological features in NGC 2371 (i.e.

the difference of the radial velocities of a feature with respect to the average radial velocity of the nebula) labelled in Fig. 2 next to their corresponding extraction regions. The outermost structures B1 and B9 have systemic radial velocities of ± 30 km s^{-1}, but the tips of the inner cavity B3 and B7 have larger systemic radial velocities of ± 70 km s^{-1}. Meanwhile, regions B4 and B6 inside the main nebular shell have systemic radial velocities of ± 40 km s^{-1} with opposite sign than those of the adjacent tips B3 and B7. The fast expansion of the bipolar lobes in NGC 2371 is consistent with the faster expansion of PNe with [WR]-type CSPNe compared to other PNe (Peña, Medina & Stasińska 2003).

The overall expansion patterns described above are consistent with those reported by Ayala et al. (2005) using longslit high-dispersion Echelle data. With that information at hand, we can envisage the simple model of the physical structure along the main nebular axis of NGC 2371 sketched in Fig. 11. The physical structure of NGC 2371 shares many similarities with that of NGC 650-1 (see Ramos-Larios et al. 2018), with two pairs of bipolar lobes tilted with the line of sight along different inclination angles, and a toroidal or barrel-like central cavity. In this geometrical model, the reversal of systemic radial velocities between the toroidal structure and the tips of the innermost bipolar lobes B3 and B7 can be explained if the toroidal structure is orthogonal to the bipolar lobes.

The present data allow a basic description of NGC 2371, but we note that the NW and SE lobes have a rich morphology that suggests a more complex structure than that proposed in Fig. 11. A complete analysis of the physical structure of NGC 2371 using information obtained along different slit positions using the Manchester Echelle Spectrograph (MES) at the 2.1 m telescope of
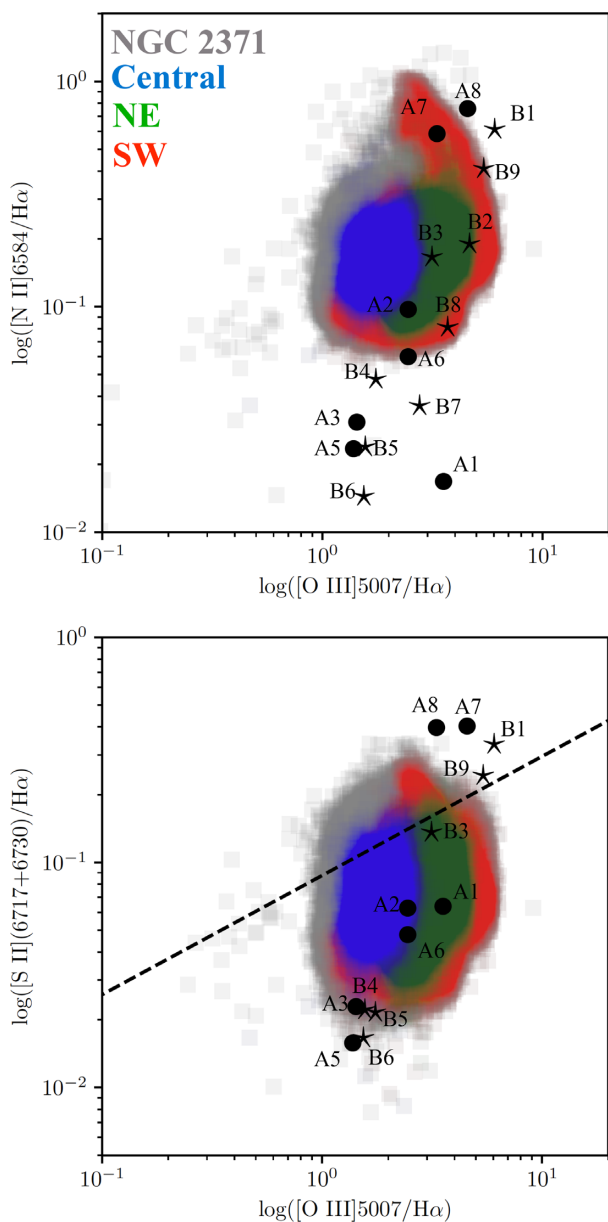
Figure 8. Line intensity ratios derived for spectra extracted from the regions in Slit A (bullets) and Slit B (stars), and from different regions of *HST* flux-calibrated ratio maps as described by the coloured points. Different colours represent line ratios extracted from the regions defined in Fig. 9, left-hand panel. The dashed line in the bottom panel marks the theoretical limit $\log([O\,III]/H\alpha) = 1.89 \times \log([S\,II]/H\alpha) + 2.46$ (see Section 4 for details) between photoionization (below the line) and shock excitation (above the line).

the Observatorio Astronómico Nacional de San Pedro Mártir (SPM-OAN) in conjunction with a morpho-kinematic model is underway (Vázquez et al. in preparation) and will certainly produce a detailed view of the physical structure of this PN to peer further into its formation history. Yet, the available data still have an interesting piece of information. The NE and SW low ionization knots move at systemic radial velocities ± 7 km s^{-1} considerably smaller than that of the toroidal structure of the main nebula where they seem to be embedded. These velocities, which are consistent with those reported by Sabbadin et al. (1982), imply that the knots are being overtaken by the nebular material as suggested by Ramos-Larios &

Phillips (2012). Furthermore, the arc-like features observed around these structures (see Fig. 1 right-hand panels) seem to suggest that they are interacting with the current fast wind from the CSPN, similarly to what is observed in *HST* images of Orion proplyds (see García-Arredondo, Henney & Arthur 2001).

5.2 A comprehensive view of NGC 2371

The spatio-kinematic model of NGC 2371 described above can be compared to its excitation structure and spatially varying chemical abundances. Despite its complex morphology, NGC 2371 is quite symmetric, with an ellipsoidal main nebular shell with polar blowouts and a pair of bipolar lobes whose symmetry axis is aligned along a slightly tilted direction. The tips of the bipolar lobes show clear evidence of shock excitation, which can arise as the nebular material expands at relatively high speed and interacts with the ISM. On the other hand, the main nebular shell and very notably the regions close to the CSPN exhibit very high excitation, with the lowest [N II]/Hα and highest He II/Hβ line ratios. Indeed, excitation in these innermost regions is so high that the [O III]/Hα line ratio is damped as O^{++} is photoionized to higher ionization levels. Furthermore, several He II emission lines can be seen in the optical spectrum shown in Fig. 5. Along with C IV and [Ne IV], it has also been reported to be present in the *IUE* UV nebular spectrum of NGC 2371 (see fig. 2 in Pottasch et al. 1981). Since the He II λ1640 Å is the dominant line in the wavelength range between 1400 and 1800 Å, the *GALEX* far-UV image in Fig. 12 (left-hand panel) can be used to probe the spatial location of high-excitation material in NGC 2371. The emission in this image traces the main morphological features of NGC 2371, including the main cavity, the dense knots, and the outer edges of the NW and SE lobes. In addition, there is a diffuse halo that extends to distances of ~70 arcsec from the CSPN, which is not detected in the near-UV *GALEX* image (see Fig. 12 right-hand panel). When comparing with mid-IR *Spitzer* presented in Ramos-Larios & Phillips (2012) and optical CFHT [O III] images, there is notable emission in the *Spitzer* images close to the CSPN, most likely associated with high-excitation [O IV] emission lines. The high excitation of the inner regions of NGC 2371 results from the strong UV flux of WD 0722+295, whereas the high excitation of the outer halo might result from the 'hardening' of the stellar radiation, as high energy photons leak from the main nebular shell of NGC 2371 (see Guerrero & Manchado 1999; Gesicki, Acker & Zijlstra 2003).

The low ionization dense SW and NE knots are aligned along a direction different from the main nebular axis and they do not share the expansion velocity of the main nebula, with lower expansion velocities (± 7 km s^{-1}). Their morphology, with bow shocks pointing towards the ionization source, also precludes a jet interpretation for these features, but they are more consistent with clumps surrounded by photoevaporated material. Thus, whereas the main nebula of NGC 2371 has very high excitation, it seems that the face of these knots pointing towards the CSPN shields their cometary tails from the UV stellar flux, producing emission from low ionization species at their tails. Indeed, the spectra extracted from these structures present emission from [O I] and [N I] (see A2, A7, and A8 in Table 2) suggesting them to be low ionization structures (LIS). The analysis of LIS in PNe presented by Akras & Gonçalves (2016) suggests $T_e = 10\,000$–$14\,700$ K, consistent with our estimates for the SW and NE knots, but lower electron densities than the surrounding ionized gas, contrary to the SW and NE knots of NGC 2371, which are much denser than the nebular material
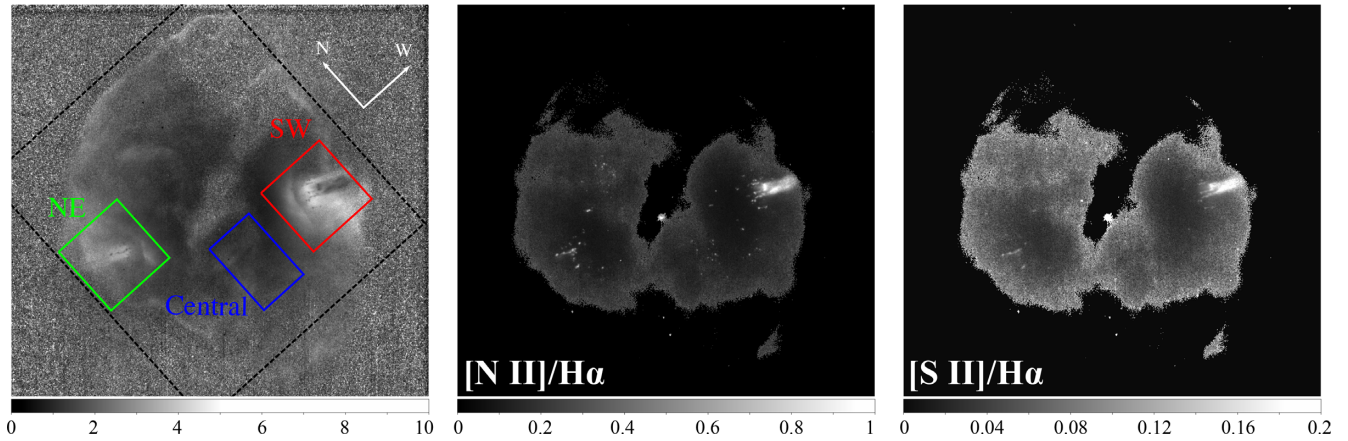
Figure 9. Line intensity ratio maps obtained from calibrated *HST* images. (*Left*) The (black) dashed line, red line, blue line, and green line rectangles represent different regions used to study the ionization structure of NGC 2371 in Fig. 8. The three panels have the same field of view and orientation.

Table 5. Total abundances for different regions in NGC 2371.

	A1	A2	A3	A5	A6	A7	A8	Solar (Lodders 2010)
He	0.106 ± 0.013	0.116 ± 0.005	0.122 ± 0.005	0.130 ± 0.006	0.118 ± 0.003	0.102 ± 0.002	0.098 ± 0.007	0.084
O	$(7.1 \pm 3.0) \times 10^{-4}$	$(3.8 \pm 1.3) \times 10^{-4}$	$(1.6 \pm 0.6) \times 10^{-4}$	$(1.7 \pm 0.7) \times 10^{-4}$	$(2.8 \pm 0.9) \times 10^{-4}$	$(6.8 \pm 2.4) \times 10^{-4}$	$(4.9 \pm 1.7) \times 10^{-4}$	5.37×10^{-4}
N	$(2.2 \pm 1.4) \times 10^{-4}$	$(1.1 \pm 0.4) \times 10^{-4}$	$(9.2 \pm 3.2) \times 10^{-5}$	$(4.7 \pm 1.7) \times 10^{-5}$	$(1.3 \pm 0.4) \times 10^{-4}$	$(2.2 \pm 0.8) \times 10^{-4}$	$(2.1 \pm 0.7) \times 10^{-4}$	7.24×10^{-5}
Ne	$(3.4 \pm 1.4) \times 10^{-4}$	$(3.4 \pm 1.0) \times 10^{-4}$	$(8.1 \pm 2.4) \times 10^{-5}$	$(1.1 \pm 0.4) \times 10^{-4}$	$(1.6 \pm 0.5) \times 10^{-4}$	$(1.4 \pm 0.4) \times 10^{-5}$	$(1.8 \pm 0.5) \times 10^{-4}$	1.12×10^{-4}
Ar	3.5×10^{-5}:	1.5×10^{-5}:	1.1×10^{-5}	5.0×10^{-6}:	1.2×10^{-5}:	1.3×10^{-5}:	9.3×10^{-6}:	3.16×10^{-6}
S	$(2.9 \pm 1.5) \times 10^{-5}$	$(7.2 \pm 2.9) \times 10^{-6}$	$(8.5 \pm 3.4) \times 10^{-6}$	$(4.4 \pm 1.8) \times 10^{-6}$	$(1.5 \pm 0.6) \times 10^{-5}$	$(1.7 \pm 0.7) \times 10^{-5}$	$(1.7 \pm 0.7) \times 10^{-5}$	1.45×10^{-5}
Cl	...	$(1.9 \pm 0.7) \times 10^{-7}$	...	...	$(3.6 \pm 1.4) \times 10^{-7}$	$(1.5 \pm 0.6) \times 10^{-7}$	...	1.78×10^{-7}
He/He$_\odot$	1.26	1.38	1.45	1.55	1.41	1.21	1.17	. . .
N/O	0.31	0.29	0.58	0.28	0.46	0.32	0.43	0.13
Ne/O	0.48	0.89	0.51	0.65	0.57	0.21	0.37	0.21
Ar/O	0.05:	0.04:	0.05:	0.03:	0.04:	0.02:	0.02:	0.006
S/O	0.04	0.02	0.05	0.03	0.05	0.03	0.03	0.03
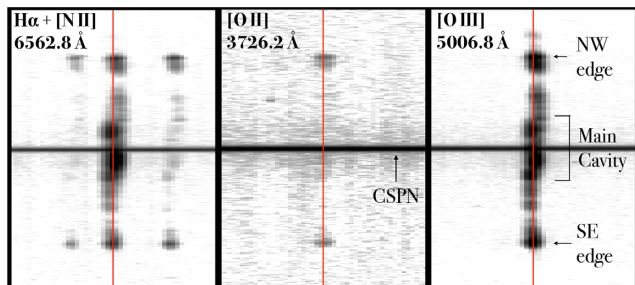
Figure 10. Sections of the INT IDS spectrum of the major axis of NGC 2371 (Slit B) centred on the H α + [N II], [O II], and [O III] lines. The red vertical lines show the position of the rest wavelength of each line. The horizontal axis represents wavelength while the vertical the spatial profile.

where they are embedded (see Table 2). In this sense, the SW and NE knots of NGC 2371 are not typical LIS.

The chemical abundances of different apertures along the minor axis of NGC 2371 are listed in Table 5. The mean value of the He abundances is 0.113 ± 0.012 ($\simeq 1.4$ times the solar value in Lodders 2010), with most individual values within 1σ uncertainty. This might also be the case for the O abundances, with a mean value of $(4.1 \pm 2.3) \times 10^{-4}$, which is mostly consistent within 1σ uncertainty with that of individual apertures. This mean value suggests slightly subsolar O abundances, (O/H) $\simeq 0.75$ (O/H)$_\odot$. On the contrary, the N abundances are clearly larger than solar, with a mean N/O ratio of 0.38 ± 0.11, i.e. (N/O) ≈ 3 (N/O)$_\odot$. The
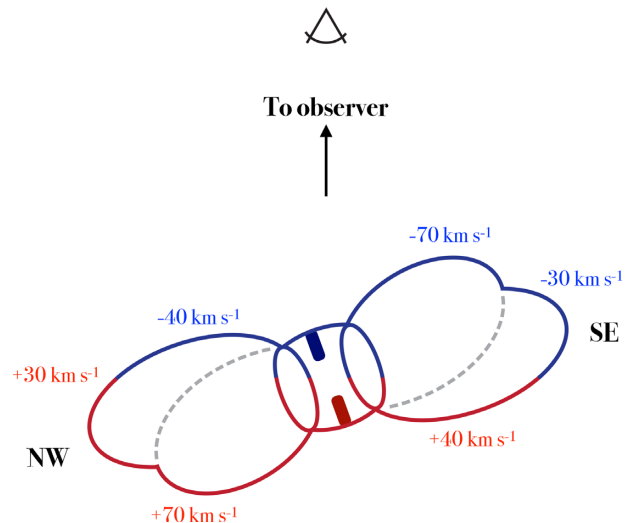
Figure 11. Velocity structure of NGC 2371 suggested by the radial velocities obtained from our spectral analysis.

chemical abundances (He/H, O/H, N/O) of NGC 2371 are basically consistent with those reported for comprehensive samples of PNe with [WC] central stars (Peña et al. 2001; García-Rojas et al. 2013). The other chemical abundances in Table 5 have larger uncertainties, particularly the Ar abundances, for which no error bar is provided.
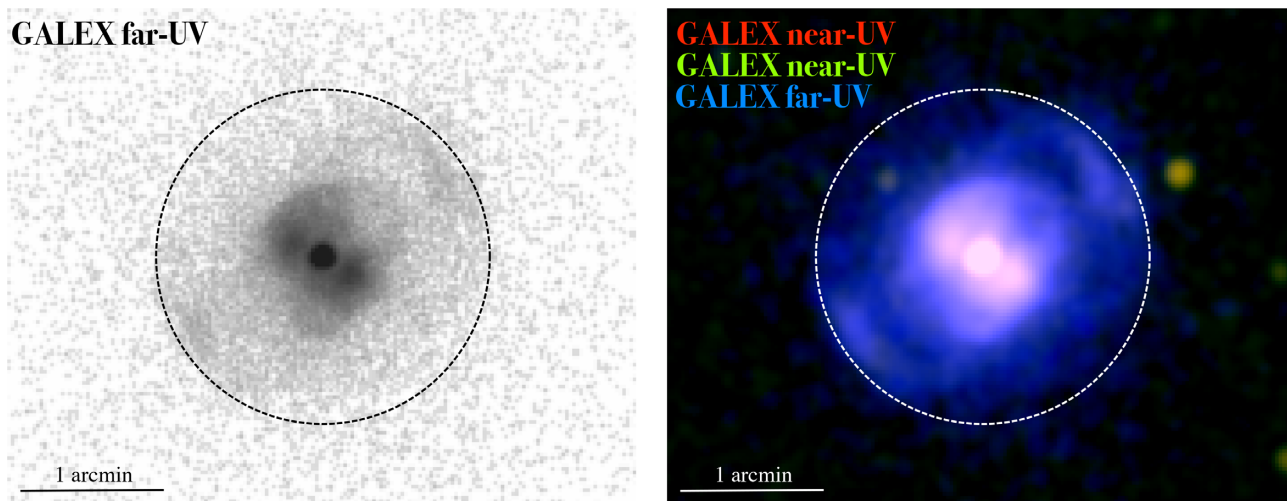
Figure 12. *GALEX* UV images of NGC 2371. (*Left*) *GALEX* far-UV grey-scale image with the natural *GALEX* pixel size of 1.5 arcsec. (*Right*) Colour-composite UV image using the near- and far-UV filters. The dashed line circle in both panels has an angular radius of 70 arcsec. North is up and east to the left.

The values of the chemical abundances of Ne, Ar, S, and Cl are also consistent with those of PNe with [WC] central stars.

The chemical abundances found in different regions are in general consistent among them, within 2σ up most from their mean values, but we note that the abundances of the main elements He, N, and O show some differences from one region to another. It might be argued that the O abundances from apertures probing the dense LIS are higher than those of the main cavity enclosing them, whereas the N/O ratios are lower. We believe this is not the case, because a close inspection reveals that the O abundances are mostly anticorrelated with T_e, underlying the difficulties to determine the chemical abundances in highly excited nebulae and from regions where low- and high-excitation material coexists.

Finally, we would like to remark that Herald & Bianchi (2004) suggested WD 0722+295 to be in the same evolutionary stage as the CSPN of the born-again PN A 78, a [WR]-PG 1159 star. Although their analysis of the stellar atmospheres of those two CSPNe with their version of the CMFGEN code resulted in similar atmospheres, our best-fitting models of WD 0722+295 and our recent analysis of the CSPN of A 78 (see Toalá et al. 2015) show these two stars to be different. Moreover, the presence of hydrogen-deficient material inside A 78 suggests a different evolutionary path compared to the CSPN of NGC 2371. The spectral analysis of WD 0722+295 presented here represents an improvement over other similar studies due to the high quality of the optical spectrum and the combination with available UV data used for the fit.

The POWR model presented here is not able to reproduce the lines identified in Section 3 at ≈ 5665 and ≈ 6066 Å as O VIIλ5666 and O VIII λ6068, because the ionization potentials of these species, 739.3 and 871.4 eV, respectively, are too high to be produced by the stellar atmosphere. Although it can be argued that such high-temperature gas can be produced by the X-ray emission of WD 0722+296 detected by *Chandra* (Montez et al. 2015), it has been long discussed whether these emission lines are due to oxygen, but to neon. Werner, Rauch & Kruk (2007) presented stellar atmosphere models of pre-WD stars and demonstrated that most of the emission lines from the O VII and O VIII high ionization states of oxygen might be misidentified with those of Ne VII and Ne VIII, whose ionization potentials, 207.3 and 239.1 eV, respectively, are considerably lower. This does not affect the spectral classification

of WD 0722+296 as part of the [WO] sequence, because the O VI λ3820, O VI λ5290, and O VI λ6200 lines are still present in its spectrum (see Table 1). Indeed, the Ne VII and Ne VIII lines require a high temperature for the central star.

6 SUMMARY

We presented spatially resolved longslit INT IDS spectroscopic observations of NGC 2371, a PN with a [WR]-type CSPN with an apparent complex morphology. Our spectral observations, in conjunction with *HST*, *GALEX*, and CFHT images, have allowed us to characterize the central star of NGC 2371 as well as to unveil its high ionization structure. Our findings can be summarized as follows:

(i) We studied the spectral properties of the CSPN of NGC 2371, WD 0722+295, by analysing the IDS observations. A Gaussian-fitting procedure was performed to measure the true contribution of the WR spectral lines and to assess the spectral subtype of the CSPN. Line ratios of WR features with that of the RB suggest a [WO1]. In combination with the UV data, we used the stellar atmosphere code POWR to estimate the stellar parameters. Although we found very similar results as those obtained in previous works, the differences are due to the assumed clumping factor and a more accurate *Gaia* distance.

(ii) We studied the physical properties of different regions of NGC 2371. In accordance with previous works on NGC 2371, the electron density ranges between 100 cm^{-3} and 1640 cm^{-4}. The densest regions are the SW and NE low ionization knots. The electron temperatures vary from $T_e \sim 12\,000$ K at the outer edges to $T_e \approx 18\,000$ K for regions close to the star. The outer bipolar (NW and SE) lobes have electron densities $n_e \approx 400$ cm^{-3} and $T_e \approx 12\,000$–$13\,000$ K.

(iii) The analysis of emission line ratios from the IDS spectra as well as those extracted from the *HST* calibrated images demonstrate the powerful effect of the UV flux from the CSPN of NGC 2371. Most emission from this PNe is dominated by ionization, but the low ionization SW and NE knots and the outer regions B1 and B9, where shock excitation is important. We suggest that B1 and B9 are shock excited because they trace the shock due to the expansion of NGC 2371.

(iv) Inspection of *GALEX* images unveiled the presence of a halo extended to 70 arcsec from WD 0722+295. The halo is detected in the far-UV channel and is mainly dominated by He II emission. We suggest that this halo has formed due to high-energy photon leakage.

(v) We found that the bow shock-like structure around the CSPN-facing head of the low ionization dense knots correspond to photoevaporation flows. The head of the knots shield their tails producing emission from low ionization species such as [O I] and [N I]. This reinforces the idea proposed by Herald & Bianchi (2004) and Ramos-Larios & Phillips (2012) that molecular material might be present in the vicinity of the CSPN of NGC 2371, probably in these structures similar to LIS in other PNe (Akras, Gonçalves & Ramos-Larios 2017). However, we note that these clumps do not share the same physical properties as classic LIS described in the literature.

(vi) We estimated the chemical abundances for different regions of NGC 2371. The abundances are typical of PNe with [WC] central stars. Although some variations may exist among different regions, the abundances of the dense knots lay within those of adjacent regions, suggesting that they were not ejected as the result of a VLTP. Instead, their kinematics and detailed morphology suggest they were ejected before the formation of the main nebular shell.

(vii) The relatively high resolution of the optical longslit spectra presented here allowed us to suggest a possible kinematic structure of NGC 2371. The outer lobes have the typical expansion velocity of evolved PNe ($\sim$30 km s^{-1}) while the inner shell has an expansion velocity of $\sim$70 km s^{-1} in accordance with previous analysis of high-resolution Echelle observations. On the other hand, the dense knots have a slow radial velocity. We suggest that NGC 2371 has a bipolar shape with each lobe presenting a double structure protruding from a barrel-like central region.

We propose that the densest material around WD 0722+295 might be the relic of an early ejection of material along a ring-like structure. The ejection of the main nebula is more recent and can be directly related to the current fast stellar wind of the progenitor star of NGC 2371. It seems to have expanded towards the low-density region, the polar zone of the barrel-like structure. We emphasize that the analysis of high-resolution Echelle observations such as those obtained with the San Pedro Mártir MES are most needed in order to construct a detailed view of the morpho-kinematic structure of NGC 2371.

ACKNOWLEDGEMENTS

REFERENCES

Acker A., Neiner C., 2003, A&A, 403, 659
Acker A., Górny S. K., Stenholm B., 1996, Ap&SS, 238, 63
Akashi M., Soker N., 2017, MNRAS, 469, 3296
Akras S., Gonçalves D. R., 2016, MNRAS, 455, 930
Akras S., Gonçalves D. R., Ramos-Larios G., 2017, MNRAS, 465, 1289
Aller L. H., Czyzak S. J., 1979, Ap&SS, 62, 397
Ayala S., Vázquez R., Miranda L. F., Olguín L., 2005, in Szczerba R., Stasińska G., Gorny S. K., eds AIP Conf. Proc. Vol. 804, Planetary Nebulae as Astronomical Tools, 804, p. 95
Bailer-Jones C. A. L., Rybizki J., Fouesneau M., Mantelet G., Andrae R., 2018, AJ, 156, 58
Balick B., 1987, AJ, 94, 671
Cardelli J. A. A., Clayton G. C., Mathis J. S., 1989, ApJ, 345, 245
Crowther P. A., De Marco O., Barlow M. J., 1998, MNRAS, 296, 367
Curtis H. D., 1918, Publ. Lick Obs., 13, 55
Danehkar A., Karovska M., Maksym W. P., Montez R., Jr., 2018, ApJ, 852, 87
De Marco O., Crowther P. A., 1999, MNRAS, 306, 931
Delgado-Inglada G., Morisset C., Stasińska G., 2014, MNRAS, 440, 536–554
García-Arredondo F., Henney W. J., Arthur S. J., 2001, ApJ, 561, 830
García-Rojas J., Peña M., Morisset C., Delgado-Inglada G., Mesa-Delgado A., Ruiz M. T., 2013, A&A, 558, A122
Gesicki K., Acker A., Zijlstra A. A., 2003, A&A, 400, 957
Gesicki K., Zijlstra A. A., Acker A., Górny S. K., Gozdziewski K., Walsh J. R., 2006, A&A, 451, 925
Gómez-González V. M. A., Mayya Y. D., Rosa-González D., Rodríguez-Merino L. H., Toalá J. A., Alvarez C., 2020, MNRAS, 493, 3879
Górny S. K., 2001, Ap&SS, 275, 67
Górny S. K., Tylenda R., 2000, A&A, 362, 1008
Gräfener G., Koesterke L., Hamann W.-R., 2002, A&A, 387, 244
Guerrero M. A., Manchado A., 1999, ApJ, 522, 378
Guerrero M. A. et al., 2018, Nat. Astron., 2, 784
Hamann W.-R., Gräfener G., 2004, A&A, 427, 697
Heap S. R., 1982, in De Loore C. W. H., Willis A. J., eds, Proc. IAU Symp. 99, Wolf-Rayet Stars: Observations, Physics, Evolution. Kluwer, Dordrecht, p. 423
Henry R. B. C., Stephenson B. G., Miller Bertolami M. M., Kwitter K. B., Balick B., 2018, MNRAS, 473, 241
Herald J. E., Bianchi L., 2004, ApJ, 609, 378
Herwig F., Blöcker T., Langer N., Driebe T., 1999, A&A, 349, L5
Hillier D. J., Miller D. L., 1998, ApJ, 496, 407
Hillier D. J., Miller D. L., 1999, ApJ, 519, 354
Jacob R., Schönberner D., Steffen M., 2013, A&A, 558, A78
Kaler J. B., Stanghellini L., Shaw R. A., 1993, A&A, 279, 529
Kwok S., Purton C. R., Fitzgerald P. M., 1978, ApJ, 219, L125
Lodders K., 2010, Astrophysics and Space Science Proceedings, Vol. 16. Springer-Verlag Berlin Heidelberg, p. 379
Luridiana V., Morisset C., Shaw R. A., 2015, A&A, 573, A42
Medina S., Peña M., Morisset C., Stasińska G., 2006, Rev. Mex. Astron. Astrofis., 42, 53
Miller Bertolami M. M., 2016, A&A, 588, A25
Miller Bertolami M. M., Althaus L. G., 2006, A&A, 454, 845

Miszalski B., Crowther P. A., De Marco O., Köppen J., Moffat A. F. J., Acker A., Hillwig T. C., 2012, MNRAS, 423, 934

Montez R. et al., 2015, ApJ, 800, 8

Osterbrock D. E., Ferland G. J., 2006, in Osterbrock D. E., Ferland G. J., eds, Astrophysics of Gaseous Nebulae and Active Galactic Nuclei. University Science Books, Sausalito, CA

Peña M., Stasińska G., Esteban C., Koesterke L., Medina S., Kingsburgh R., 1998, A&A, 337, 866

Peña M., Stasińska G., Medina S., 2001, A&A, 367, 983

Peña M., Medina S., Stasińska G., 2003, in Arthur J., Henney W. J., eds, Revista Mexicana De Astronomia Y Astrofisica Conference Series, 15, p. 38

Peña M., Rechy-García J. S., García-Rojas J., 2013, Rev. Mex. Astron. Astrofis., 49, 87

Pottasch S. R., Gathier R., Gilra D. P., Wesselius P. R., 1981, A&A, 102, 237

Press W. H., Teukolsky S. A., Vetterling W. T., Flannery B. P., 1992, Numerical recipes in FORTRAN. The Art of Scientific Computing. Cambridge Univ. Press, Cambridge

Raga A. C., Riera A., Mellema G., Esquivel A., Velázquez P. F., 2008, A&A, 489, 1141

Ramos-Larios G., Phillips J. P., 2012, MNRAS, 425, 1091

Ramos-Larios G. et al., 2018, MNRAS, 475, 932

Rechy-García J. S., Velázquez P. F., Peña M., Raga A. C., 2017, MNRAS, 464, 2318

Rechy-García J. S., Peña M., Velázquez P. F., 2019, MNRAS, 482, 1163

Sabbadin F., Bianchini A., Hamzaoglu E., 1982, A&AS, 50, 523

Sahai R., Morris M. R., Villar G. G., 2011, AJ, 141, 134

Smith L. F., Aller L. H., 1969, ApJ, 157, 1245

Toalá J. A. et al., 2015, ApJ, 799, 67

Toalá J. A., Ramos-Larios G., Guerrero M. A., Todt H., 2019, MNRAS, 485, 3360

Todt H., Peña M., Hamann W.-R., Gräfener G., 2010, A&A, 515, A83

Todt H. et al., 2013a, MNRAS, 430, 2302

Todt H., Peña M., Hamann W.-R., Gräfener G., 2013b, 18th European White Dwarf Workshop. p. 303

Todt H., Sander A., Hainich R., Hamann W.-R., Quade M., Shenar T., 2015, A&A, 579, A75

Tody D., 1993, in Hanisch R. J., Brissenden R. J. V., Barnes J., eds, ASP Conf. Ser. Vol. 52, Astronomical Data Analysis Software and Systems II. Astron. Soc. Pac., San Francisco, p. 173

Torres-Peimbert S., Peimbert M., 1977, Rev. Mex. Astron. Astrofis., 2, 181

Tylenda R., Acker A., Stenholm B., 1993, A&AS, 102, 595

Werner K., Rauch T., Kruk J. W., 2007, A&A, 474, 591

Zijlstra A. A., 2015, Rev. Mex. Astron. Astrofis., 51, 221

This paper has been typeset from a TʷX/LἶTʷX file prepared by the author.